# Interaction of $(La_{1-x}Sr_x)_nCo_{1-y}Fe_yO_{3-\delta}$ cathodes and AISI 441 interconnect for solid oxide fuel cells

Wenle Li [1], Kathy Lu*, Zhenbo Xia [2]

Department of Materials Science and Engineering, Virginia Tech, VA 24061, USA

## HIGHLIGHTS

- AISI 441/LSCF reaction is associated with cathode microstructure and diffusion.
- LSCF composition affects microstructural evolution and element diffusion.
- Chromium diffusion varies with A-site availability in LSCF perovskite structure.
- Mechanisms governing ohmic and frequency polarization resistances are discussed.
- A-site deficient perovskite LSCF structure improves the performance of the cathode.

## GRAPHICAL ABSTRACT
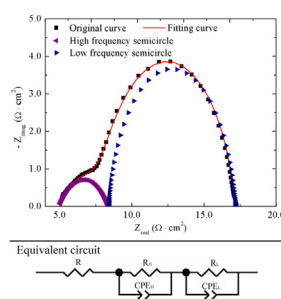
## ABSTRACT

Material degradation is a major issue for solid oxide fuel cells servicing under severe high temperature environments. This work studies the interaction between $(La_{1-x}Sr_x)_nCo_{1-y}Fe_yO_{3-\delta}$ (LSCF) cathode and AISI 441 alloy interconnect at 800 °C by investigating the interfacial reaction and degradation through an AISI 441 interconnect/LSCF electrode/yttria-stabilized zirconia (YSZ) electrolyte tri-layer structure. LSCFs with different stoichiometries are created in order to understand cathode composition effect on solid oxide fuel cell performance. The porous microstructures of the electrodes experience significant evolution after the thermal treatment under current load. Energy dispersive X-ray spectroscopy and X-ray photoelectron spectroscopy analyses reveal the significance of elemental distributions on the performance of the cathodes. Cr, La, and Co distributions vary with stoichiometry. Ohmic resistance and polarization resistance of the cathodes are analyzed by deconvoluting the electrochemical impedance spectroscopy (EIS) results. Based on the elemental distribution, the microstructure evolution of the LSCF electrodes, and the EIS analysis, the interaction mechanisms between the LSCF electrodes and the AISI 441 alloy are proposed. Overall, the A-site deficient stoichiometry is preferred.

© 2013 Elsevier B.V. All rights reserved.

* Corresponding author. 211B Holden Hall, Materials Science and Engineering Department, Virginia Tech, Blacksburg, VA 24061, USA. Tel.: +1 540 231 3225; fax: +1 540 231 8919.
  E-mail addresses: wenle@vt.edu (W. Li), klu@vt.edu (K. Lu), zxia@vt.edu (Z. Xia).
[1] 127 Randolph Hall, Materials Science and Engineering Department, Virginia Tech, Blacksburg, VA 24061, USA. Tel.: +1 540 266 8020; fax: +1 540 231 5022.
[2] 211B Holden Hall, Materials Science and Engineering Department, Virginia Tech, Blacksburg, VA 24061, USA. Tel.: +1 540 808 9758; fax: +1 540 231 8919.

## 1. Introduction

Known for its high efficiency, ability to generate electricity from hydrocarbon fuels, low level of pollutants, and high power density [1], solid oxide fuel cell (SOFC) has been extensively studied in the past three decades. Several materials have been studied as the cathode, including $(La,Sr)MnO_3$ [2], $La(Ni,Fe)O_3$ [3], $(La,Sr)_2NiO_4$ [4],

(La,Sr)MO$_3$ (M = Cr, Fe, Co), and (La,Ca)CoO$_3$ [5,6]. Lanthanum strontium cobaltite ferrite (La$_{1-x}$Sr$_x$Co$_{1-y}$Fe$_y$O$_{3-\delta}$, LSCF) is a promising cathode candidate for several reasons [7,8]. Specifically, LSCF possesses high electronic-ionic mixed conductivity [9,10], low polarization resistance [11,12], high oxygen semi-permeability [13], and high catalytic activity for O$_2$ reduction reaction [14]. In addition, investigations on chromium poisoning suggest that LSCF is a more Cr-tolerant cathode than other materials, e.g. (La,Sr)MnO$_3$ [15–17]. Among LSCF electrodes with different stoichiometries, La$_{0.6}$Sr$_{0.4}$Co$_{0.2}$Fe$_{0.8}$O$_3$ is the most recognized composition, owing to its balanced properties [14]: >250 S cm$^{-1}$ conductivity at 800 °C [18], 0.33 $\Omega$ cm$^2$ polarization resistance at 600 °C [19], and 17.5 $\times$ 10$^{-6}$ K$^{-1}$ thermal expansion coefficient from 30 °C to 1000 °C [20].

LSCF is a typical perovskite ABO$_3$ electrode, with La$^{3+}$ and Sr$^{2+}$ occupying A-site and Co$^{3+}$ and Fe$^{3+}$ occupying B-site. The substitution of La$^{3+}$ by Sr$^{2+}$ generates either B$^{4+}$ ions or oxygen vacancies to maintain the charge neutrality of the oxide [18]. In order to improve the performance of the electrode, A-site deficient LSCF has been introduced as additional oxygen vacancies can be generated by the A-site deficiency and consequently improve the ion conductivity [21–24]. In contrast, A-site excessive LSCF is seldom investigated.

Despite the advantages of LSCF-based cathode, several issues are associated with the current studies and the cathodes are far from being optimized. One most important problem is the material degradation caused by the interaction between the metallic interconnect and the cathode. In the past decades, considerable investigations have been carried out to understand the mechanism of chromium migration between the metallic interconnect and the cathode and several theories were proposed [3,25–27]. For example, Badwal et al. and Taniguchi et al. suggest that Cr deposition is determined by oxygen activity at the triple phase boundaries [28,29]; while Konysheva et al. believe that material degradation is induced by loss of electrochemically active sites and decomposition of the cathode [15]. Apparently, agreement regarding the chromium migration and deactivation of the cell has not been reached and further exploration is required [3]. In addition, LSCF has been reported to form SrZrO$_3$ insulating phase with ZrO$_2$ from the electrolyte (i.e. yttria stabilized zirconia, YSZ) and compromise cell performance [19,30].

In this study, LSCF-based cathodes with different stoichiometry are fabricated. Synthesized La$_{0.6}$Sr$_{0.4}$Co$_{0.2}$Fe$_{0.8}$O$_3$ (noted as LSCF 100), (La$_{0.6}$Sr$_{0.4}$)$_{0.95}$Co$_{0.2}$Fe$_{0.8}$O$_3$ (A-site deficient, noted as LSCF 95), and (La$_{0.6}$Sr$_{0.4}$)$_{1.05}$Co$_{0.2}$Fe$_{0.8}$O$_3$ (A-site excessive, noted as LSCF 105) are used as cathode to study the interconnect-electrode interfacial reaction and degradation with YSZ and AISI 441 alloy serving as the electrolyte and the interconnect, respectively. The microstructures of the as-prepared and the thermally treated LSCFs are characterized and the electrochemical performance of the cathodes is examined. The interactions of the AISI 441/LSCF/YSZ half-cell are analyzed. Based on these efforts, the cathode degradation mechanism is proposed.

## 2. Experimental procedures

### 2.1. Synthesis of LSCF powder

In this work, perovskite LSCF powder was synthesized by a solid state reaction process [31]. La$_2$O$_3$ (Alfa Aesar, Ward Hill, MA), SrCO$_3$ (Sigma–Aldrich, St. Louis, MO), Co$_3$O$_4$ (Alfa Aesar, Ward Hill, MA), and Fe$_2$O$_3$ (Sigma–Aldrich, St. Louis, MO) were used as-received to synthesize perovskite LSCF. The mixed powders (three compositions were made based on the stoichiometric ratio: LSCF 95, LSCF 100, and LSCF 105) were ball-milled overnight and then sintered at 1400 °C for 15 h with a heating and cooling rate of 5 °C min$^{-1}$. The resulting powders were ball-milled overnight again to reduce the

particle size, and a second sintering process at 1400 °C for 5 h was carried out with the same heating and cooling rate. The prepared powders were then ball-milled for 3 days to further reduce the particle size and improve the performance of the resulting cathodes.

### 2.2. Assembly of AISI 441/LSCF/YSZ tri-layer

The LSCF powders (56.8 wt%) were mixed and ball-milled with microcrystalline cellulose (pore-forming agent, 5.7 wt%, Spectrum, Gardena, CA), ethyl cellulose (binder, 1.1 wt%, Acros Organics, New Jersey), and $\alpha$-terpineol (solvent, 36.4 wt%, Sigma–Aldrich, St. Louis, MO) for 1 h to make pastes for screen printing. The prepared pastes were screen printed on 8 mol% YSZ (Nextech Materials, Lewis Center, OH) substrates, using a #330 mesh. The screen printed pastes were square-like with a 0.5 cm$^2$ area. The LSCF/YSZ couples were kept at 200 °C for 3 h and at 400 °C for 1 h to burn out the binder, pore-forming agent, and solvent. Afterward, these bi-layers were sintered at 1150 °C for 2 h, with a heating and cooling rate of 1 °C min$^{-1}$. The thickness of the LSCF electrodes after sintering was ~20 μm, measured through scanning electron microscopy (SEM) images.

AISI 441 ferritic stainless steel pieces (ATI Allegheny Ludlum Corporation, Brackenridge, PA) were used as interconnect material and were cut into rectangular substrates (area: 25.4 $\times$ 25.4 mm$^2$, thickness: 2.08 mm). In order to remove the oxidized layer (if any) and obtain a scratch free flat surface, the steel pieces were polished to optical finish, and ultrasonically cleaned with water and ethanol. The polished AISI 441 alloy piece was placed on the LSCF electrode side of the LSCF/YSZ bi-layer and the configuration of the tri-layer was shown in our previous paper [32].

### 2.3. Thermal treatment under current load

In order to investigate the electrochemical behavior of the LSCF cathodes, AISI 441/LSCF/YSZ tri-layers were heated to 800 °C, using a tube furnace (1730-20 HT Furnace, CM Furnace Inc. Bloomfield, NJ) in dry air environment. Afterward, the tri-layers were cathodically polarized under a constant current density of 200 mA cm$^{-2}$, using a potentiostat (VersaSTAT 3, Princeton Applied Research, Oak Ridge, TN). A platinum mesh was placed in-between the LSCF porous layer and the AISI 441 interconnect to optimize the current distribution, and the electrodes were connected by Pt wires along with Pd paste. The electrochemical impedance spectroscopy (EIS) testing program used was a multi-loop process. In each loop, EIS was test from 100 kHz to 0.025 Hz. The amplitude was 10 mV. After that, a current density of 200 mA cm$^{-2}$ was applied to mimic the working condition of the fuel cell. EIS data were recorded every 5 h during the thermal treatment.

### 2.4. Characterization & performance

The microstructures of the synthesized LSCF powders and the cathode (both cross-section and top surface) were examined by a field emission SEM (LEO1550, Carl Zeiss MicroImaging Inc., Thornwood, NY), with a 3 nm Au–Pt layer coating applied before imaging. The phase development of the synthesized LSCFs was carried out by X-ray diffraction (XRD, X'Pert PRO diffractometer, PANalytical B.V., EA Almelo, The Netherlands). The particle size of each powder was measured by a laser light scattering analyzer (LA-750, Horiba Ltd., Japan). The energy dispersive X-ray spectroscopy module (EDS, Bruker AXS, MiKroanalysis Gmbh, Berlin, Germany) attached to the SEM and X-ray photoelectron spectroscopy (XPS, PHI Quantera SXM, ULVAC-PHI Inc., Kanagawa, Japan) were used to analyze elemental distributions throughout the cathodes after the EIS test.

## 3. Results and discussion

### 3.1. Characteristics of the LSCF cathodes

The phases of the synthesized LSCF powders are obtained as shown in Fig. 1a. All of the synthesized LSCF powders, regardless of the stoichiometry, show clean perovskite crystal phase. It means that the 5% difference in the stoichiometry is too small to generate any additional detectable crystal phase. This is also desirable for studying the stoichiometry effect of the cathode on the half-cell performance as the cathode crystal structure can be eliminated as a variable.

Particle sizes of the synthesized LSCF powders have been carefully considered during this study as it greatly influences the homogeneity of the screen printing pastes, porosity and microstructure of the screen-printed LSCF layers, and therefore the performance of the cathodes. Two-step sintering and long-time ball milling are intended to reduce both the particle size and size distribution. As shown in Fig. 1b, all of the three samples have an average particle size of ∼1 μm. The three profiles of the size distribution are very similar to each other; therefore, any difference among the properties of the cathodes is caused by the stoichiometry difference.

The microstructures of the screen-printed and sintered LSCF electrode surfaces are shown in Fig. 1c. All of the LSCF electrode layers have porous microstructure. The porosities of all three LSCF cathodes are approximately 40%, roughly estimated by the known compositions and measured geometries/weights. From LSCF 95, to LSCF 100, and to LSCF 105, both the grain size and pore size increase

gradually while the morphology of the grains is conserved. This indicates that higher A-site composition LSCFs are easier to sinter and lose grain surfaces more easily at high temperatures. Although the samples with different stoichiometry have very close porosities, in LSCF 95, a large amount of grain boundaries exists and grains are highly connected. As for LSCF 100, grains become less connected and the amount of grain boundaries decreases. The least connected grains are found in LSCF 105, where the grains are connected mostly by small bridges instead of continuous grain boundaries. In contrast, the pores become more interconnected from LSCF 95, to LSCF 100, and to LSCF 105.

### 3.2. Electrochemical behaviors

Impedance spectra of all three LSCF cathodes after 5 h, 50 h, and 100 h of thermal treatment are plotted in Figs. 2a–c, respectively. The data points in-between the above time points show consistent trend and are omitted for clarity. As shown, the curve for LSCF 95 has a more ideal semi-circle shape, while the curves for LSCF 100 and LSCF 105 display asymmetric shapes with small shoulders appearing at the lower left corner of the plots. The shapes of the curves are conserved for the entire thermal treatment duration, and the only change is that the shoulders for the LSCF 100 and LSCF 105 samples grow with time. As for the impedance values, LSCF 100 has the smallest semi-circle during the entire thermal treatment process. Also, all the semi-circles shrink with time (i.e. the left intercepts on the horizontal axis are roughly fixed while the right
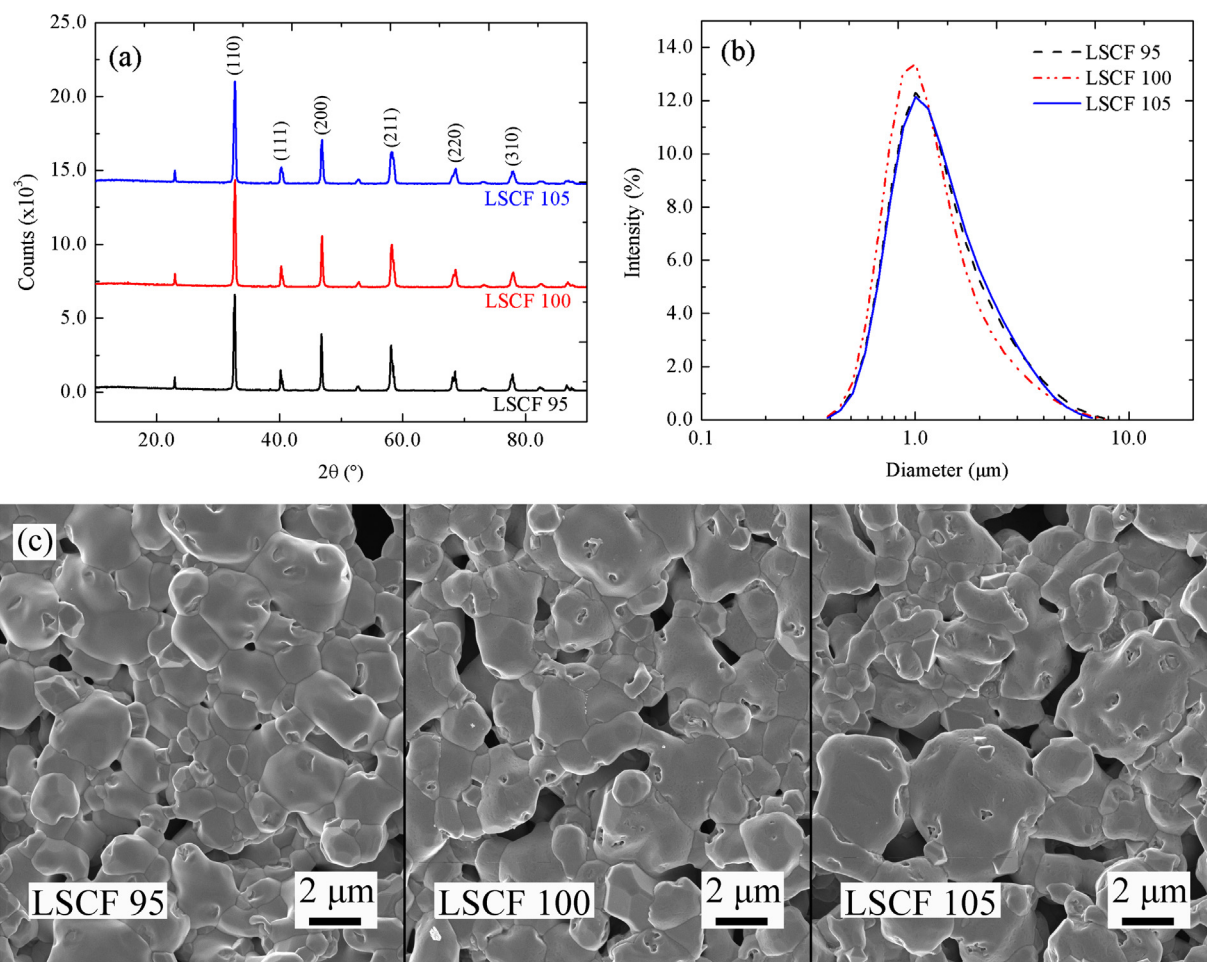


**Fig. 1.** (a) X-ray diffraction patterns of the synthesized LSCF powders. (b) Particle size distribution of the as-prepared LSCF powders (each plot is the average of three measurements). (c) Microstructures of the screen printed and sintered LSCF electrodes.
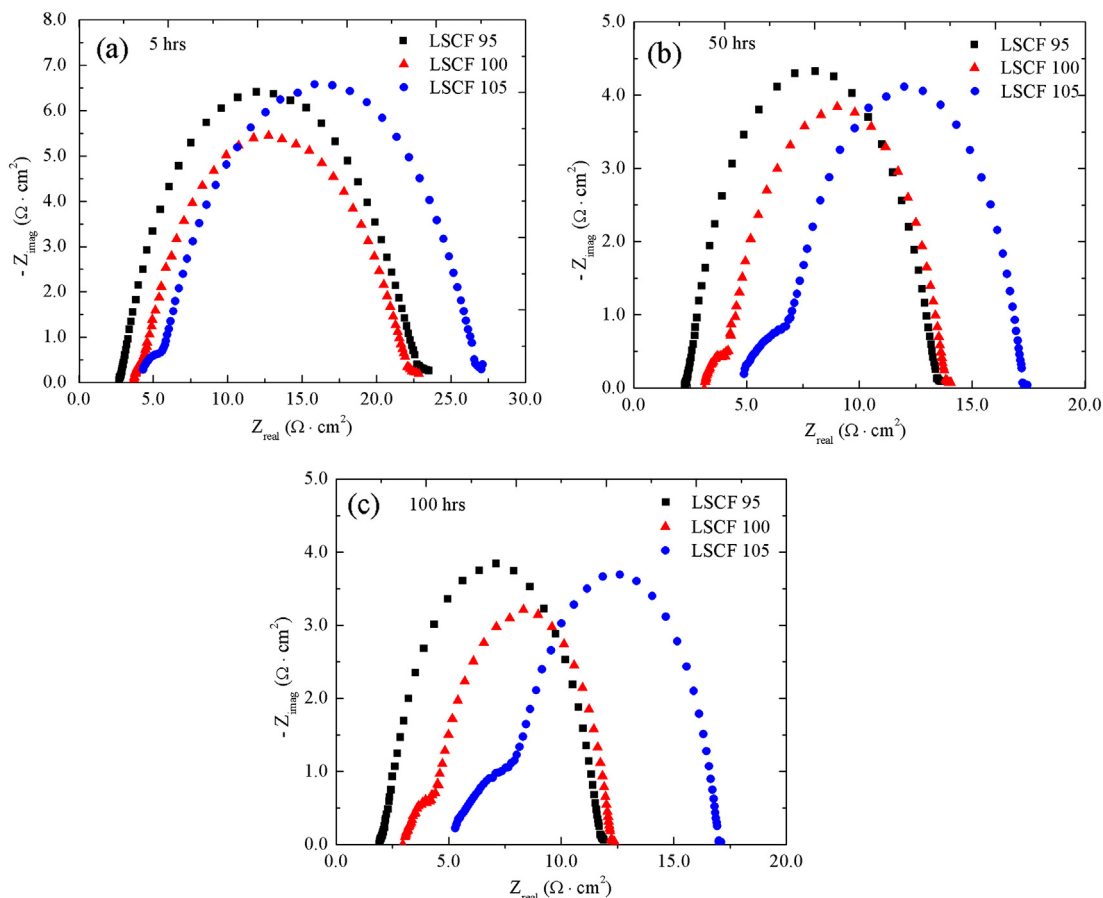
**Fig. 2.** Impedance spectra of LSCF electrodes (LSCF 95, LSCF 100, and LSCF 105) under 200 mA cm$^{-2}$ current load after thermal treatment for: (a) 5 h, (b) 50 h, and (c) 100 h.

ones become smaller for each plot, the heights of the curves also decrease). During the test, the decreasing rates of the semi-circles are different from each other. As a result, the right intercepts on the horizontal axis for LSCF 95 and LSCF 100 switch positions after ∼25 h of thermal treatment (plot not shown for brevity).

In order to correlate the EIS spectra with the mechanisms of the LSCF cathode evolution, equivalent circuit $R_\Omega(R_H CPE_H)(R_L CPE_L)$ (Insert of Fig. 3) was used to fit the spectra and obtain deconvoluted arcs at different frequencies (the spectrum for LSCF 105 after 80 h of thermal treatment is deconvoluted and shown in Fig. 3 as an example). This equivalent circuit was developed in consideration of previously proposed ones [2,10,33] and the properties of the studied cathodes (morphology of the spectra and porosity of the electrodes). In the circuit, $R_\Omega$ is the ohmic resistance from the cathode, the Pt wires, and the Pd paste; $R_H$ and $R_L$ refer to the polarization resistances at high and low frequencies, while $CPE_H$ and $CPE_L$ are constant phase elements corresponding to each frequency range. The values for each resistance are listed in Table 1 with more data points from the thermal treatment.

As shown, all resistances (ohmic resistance, high frequency polarization resistance, and low frequency polarization resistance) decrease with time for the LSCF 95 cathode. In comparison, ohmic resistance slightly decreases initially and then becomes stabilized for the LSCF 100 cathode, while the high frequency polarization resistance gradually increases. The low frequency polarization resistance for LSCF 100 continuously decreases. For LSCF 105, the low frequency polarization resistance also decreases continuously, but the ohmic resistance and the high frequency polarization resistance keep increasing with the thermal treatment time.

For different LSCF stoichiometries, the ohmic resistance increases from LSCF 95, to LSCF 100, and to LSCF 105. The values
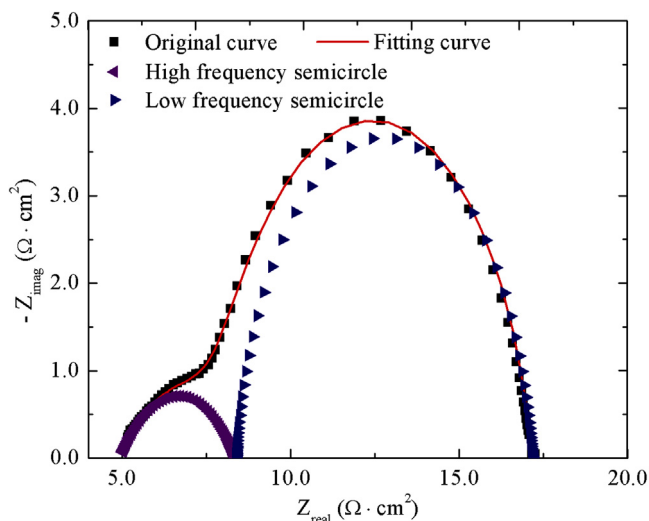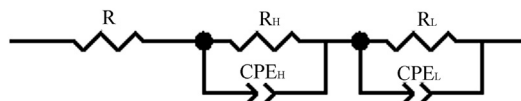


**Fig. 3.** Example of deconvolution of the impedance spectra (80 h thermal treated LSCF 105). Insert shows the equivalent circuit used for fitting the spectra.

**Table 1**
Resistance values of the cathodes derived from fitting of the impedance spectra.

| Thermal treatment time (h) | LSCF 95 | | | LSCF 100 | | | LSCF 105 | | |
|---|---|---|---|---|---|---|---|---|---|
| | $R_\Omega$ ($\Omega$) | $R_H$ ($\Omega$) | $R_L$ ($\Omega$) | $R_\Omega$ ($\Omega$) | $R_H$ ($\Omega$) | $R_L$ ($\Omega$) | $R_\Omega$ ($\Omega$) | $R_H$ ($\Omega$) | $R_L$ ($\Omega$) |
| 5 | 2.71 | 4.86 | 15.92 | 3.67 | 0.39 | 18.12 | 4.13 | 1.29 | 21.51 |
| 20 | 2.41 | 2.79 | 13.63 | 3.34 | 0.81 | 13.42 | 4.36 | 1.86 | 12.22 |
| 40 | 2.19 | 1.84 | 10.50 | 3.14 | 0.96 | 10.39 | 4.63 | 2.43 | 10.45 |
| 60 | 2.03 | 1.67 | 9.29 | 2.94 | 1.05 | 8.97 | 4.76 | 2.77 | 9.60 |
| 80 | 1.92 | 1.59 | 8.82 | 3.08 | 1.27 | 8.49 | 4.93 | 3.43 | 8.80 |
| 100 | 1.88 | 1.59 | 8.47 | 2.99 | 1.55 | 7.67 | 5.04 | 3.78 | 8.16 |

change approximately from 2 $\Omega$, to 3 $\Omega$, and then to more than 4 $\Omega$. The difference in the ohmic resistance between LSCF 95 and LSCF 100 is roughly consistent (in the 0.9 $\Omega$–1.1 $\Omega$ range), meaning that the decreasing rates of the ohmic resistances for the two electrodes are approximately the same. Since the evolution of the ohmic resistance for LSCF 105 goes in the other direction (increasing), the differences from LSCF 95 and LSCF 100 naturally keep increasing. For the initial high frequency polarization resistance, LSCF 95 has the largest value while LSCF 100 has the smallest one. As the thermal treatment time continues, the high frequency polarization resistance decreases for LSCF 95 but increases for LSCF 100 and LSCF 105. After 100 h, LSCF 95 and LSCF 100 electrodes have very close high frequency polarization resistances. LSCF 105 has an intermediate initial high frequency polarization resistance. Since the absolute increase at each time interval is higher, LSCF 105 has the largest high frequency polarization resistance after 100 h of thermal treatment. The low frequency polarization resistances decrease regardless of the stoichiometric differences. The initial values show an increasing order from LSCF 95, to LSCF 100, and to LSCF 105, but the resistances after 100 h of thermal treatment are very close to each other (i.e. between 7.6 $\Omega$ and 8.5 $\Omega$).

Overall, LSCF 95 stoichiometry is preferred as it displays the smallest ohmic resistance in a decreasing trend; its high frequency polarization resistance keeps decreasing instead of increasing; and the low frequency polarization resistance also decreases with small absolute values in general. In addition, LSCF 95 is the only composition that shows decreases in all three resistances ($R_\Omega$, $R_H$, and $R_L$). This phenomenon suggests promising performance of LSCF 95 for a long period.

### 3.3. AISI 441/LSCF/YSZ tri-layer interaction

#### 3.3.1. Microstructure evolution

Fig. 4 shows the SEM images of the interfacial surface of the LSCF cathodes in contact with AISI 441 after 100 h of thermal treatment. Although the trend for the grain sizes does not change compared to that before the thermal treatment (grain size increases gradually from LSCF 95, to LSCF 100, and to LSCF 105) and the porous microstructures are conserved during the thermal treatment, significant differences are identified in the microstructure morphologies.

After 100 h of thermal treatment, rounded grains evolve into angular polyhedrons. The grain shapes do not follow a specific description and have different geometries and numbers of facets. The LSCF 95 sample has more small grains (less than 2 µm) while the LSCF 105 sample has mostly large grains; the LSCF 100 sample has a mix of large and small grains. The number of grains correspondingly decreases from LSCF 95, to LSCF 100, and to LSCF 105 with the grain size increase. Surprisingly, the grain sizes decrease for each electrode compared to those before the thermal treatment (Fig. 1c). This means that the thermal treatment under current load (and thus the SOFC operating conditions) actually fractures LSCF grains. LSCF grain break-up should have contributed significantly to

the resistance changes seen in Table 1. Among the grains, there is a remarkable group with general tetrahedron morphology but much smaller size that behaves like shoots growing out of larger grains. These tetrahedrons are most apparent in LSCF 105, while the sizes are larger and the number is smaller in LSCF 100. Numerous tetrahedrons can also be found in LSCF 95, though they are not as obvious since they are scattered among other small grains. The inserts in Fig. 4 display a closer view of the grains, from which the primary sizes of the tetrahedrons are estimated to be ∼200 nm for LSCF 95, ∼800 nm for LSCF 100, and ∼300 nm for LSCF 105.

Another significant phenomenon regarding the microstructures is the facets on the surfaces of the grains, especially for the LSCF 95 and LSCF 105 samples, which makes the grains look like rain-scoured mountain tops.

In general, the connectivities of the microstructures of the electrodes are all improved after the thermal treatment, as the grain size decreases and the number of grain boundaries increases.

#### 3.3.2. Elemental analysis

The elemental distributions for the LSCF electrodes at the AISI 441/LSCF interface after 100 h of thermal treatment are characterized by EDS mapping. The full set of EDS mapping images is available in Supplementary data: S1 (LSCF 95), S2 (LSCF 100), and S3 (LSCF 105), respectively. The distributions of the elements are depicted by colors. The red color represents Cr, which deposits on the LSCF electrode from the chromia-forming AISI 441 alloy. The distribution of the diffused Cr varies with LSCF stoichiometry. In comparison, the Cr in LSCF 95 (Fig. 5a) is more uniformly dispersed throughout the electrode surface, while Cr in LSCF 100 (Fig. 5b) and LSCF 105 (Fig. 5c) is more concentrated (at the grain areas closer to AISI 441, high locations in the images). The overall Cr distribution for each sample agrees with that of Sr (color in blue) (Fig. 5b and d).

La (color in green) and Fe (color in purple (in the web version)) share the same elemental distribution trend (Fig. 6c and d). The La rich areas are also rich in Fe (note: La distribution in LSCF 95 is mostly consistent with that of Fe, while having some overlap with that of Cr in certain locations (Figs. 5a and 6a)). The overall elemental distribution is uniform for both species for the LSCF 95 (Fig. 6a) sample but evolves into particle-like morphology when A-site species become more available (LSCF 100 and LSCF 105) (Fig. 6c and d). It should be mentioned that La and Fe distributions are largely complementary to those of Cr and Sr; the Sr- and Cr-rich regions are La- and Fe-deficient (Figs. 5b and d, 6c and d).

The distribution of element Co (color in light blue) itself falls into the third group (Fig. 6b). It always concentrates in the regions that are Sr- or Cr-poor. However, its distribution does not always line up with those of La or Fe. In LSCF 95, again, Co is not as concentrated as in LSCF 100 and LSCF 105, but more widely dispersed over a slightly larger area. In LSCF 100 and LSCF 105, Co prefers to occupy the regions where the tetrahedral grains reside. In addition, Co distribution in LSCF 95 has some overlap with that of Fe element.

This analysis on elemental distribution at the AISI 441/LSCF interfaces confirms that species diffuse during the thermal treatment and explains the dramatic morphology changes of the LSCF electrodes. However, it should be mentioned that either there are no new phases formed yet or the amounts of new phases are too small to be detected as no additional crystal phase other than LSCF is detected by XRD after the thermal treatment. Despite the obvious elemental re-distributions in the EDS analysis, it is not significant enough to form substantial amounts of new phases yet.

Chromium diffusion from the AISI 441 surface to the LSCF electrode was also examined by XPS. Results from both EDS and XPS are shown in Table 2 for comparison. As seen, the Cr concentrations are dramatically higher in the XPS measurement than in the EDS analysis. Since XPS technique is more sensitive for surface composition
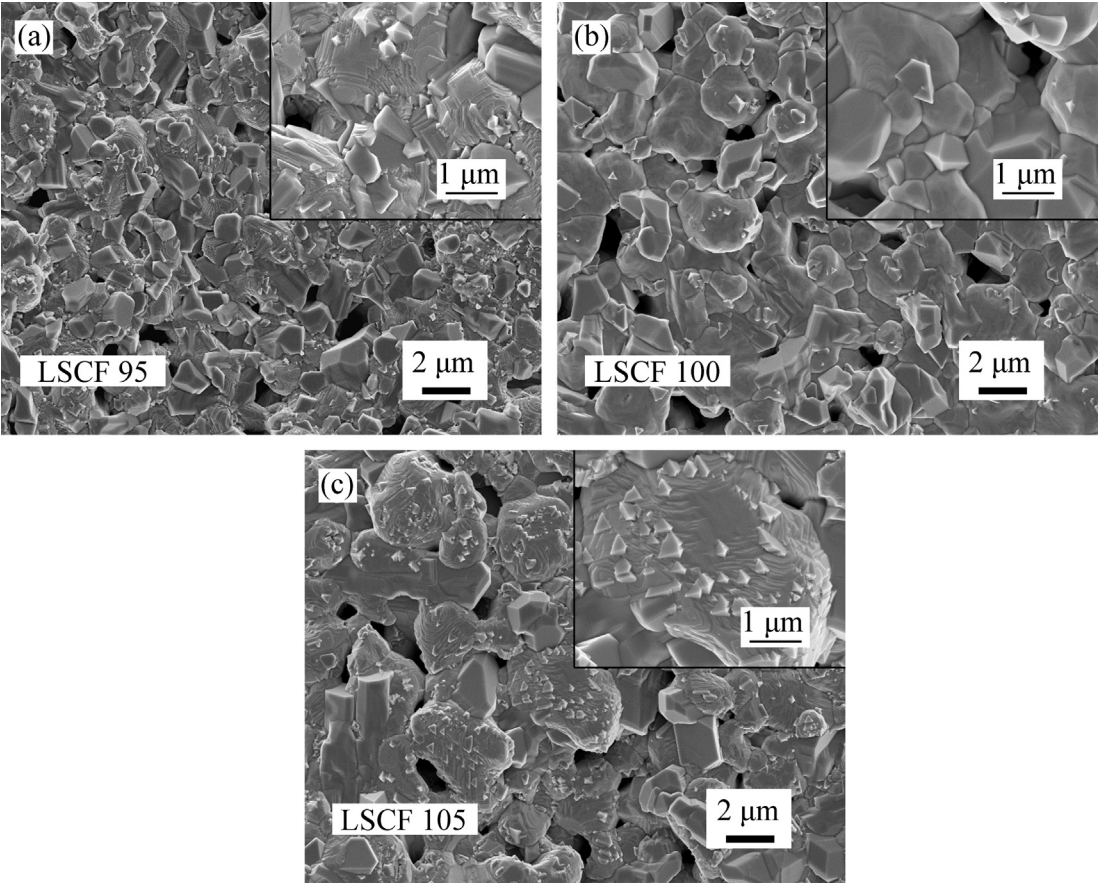
**Fig. 4.** Microstructures of the top surfaces (i.e. the surface in contact with AISI 441) of LSCF electrodes after 100 h of thermal treatment under current load: (a) LSCF 95, (b) LSCF 100, and (c) LSCF 105.
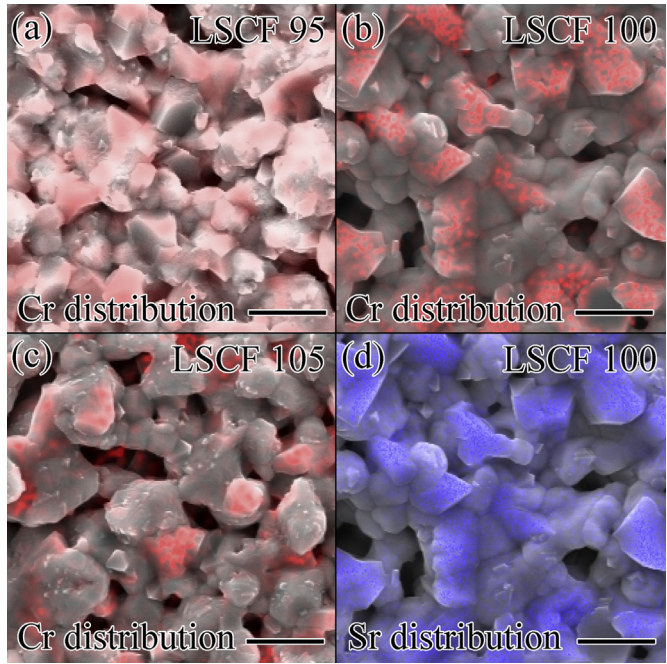


**Fig. 5.** EDS mapping showing elemental distributions of thermally treated electrode top surface: (a) Cr distribution of LSCF 95, (b) Cr distribution of LSCF 100, (c) Cr distribution of LSCF 105, and (d) Sr distribution of LSCF 100. The scale bar represents 3 μm in all the images.
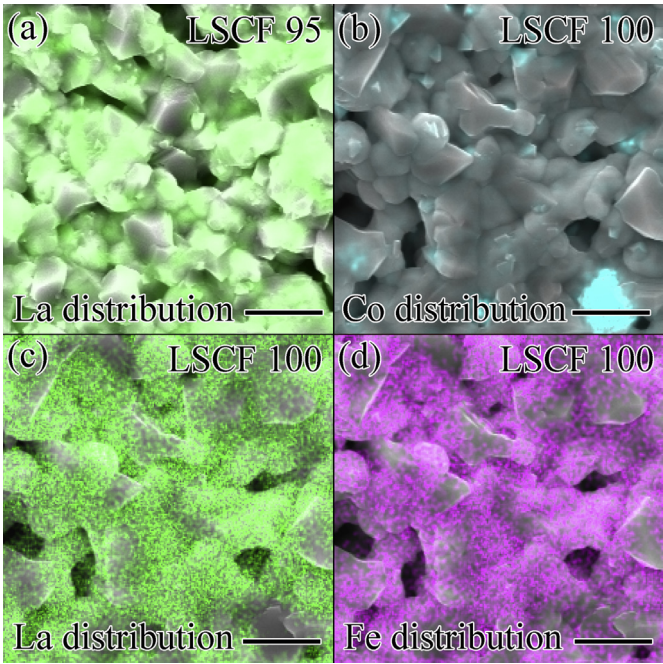


**Fig. 6.** EDS mapping showing elemental distributions of thermally treated electrode top surface: (a) La distribution of LSCF 95, (b) Co distribution of LSCF 100, (c) La distribution of LSCF 100, and (d) Fe distribution of LSCF 100. The scale bar represents 3 μm in all the images.

**Table 2**
Chromium concentration in the LSCF electrodes measured by EDS and XPS.

| Electrode | Detected by EDS (wt%) | Detected by XPS (wt%) |
| --- | --- | --- |
| LSCF 95 | 2.71 ± 0.28 | 6.99 ± 1.00 |
| LSCF 100 | 2.06 ± 0.15 | 5.89 ± 0.86 |
| LSCF 105 | 2.44 ± 0.18 | 6.75 ± 0.89 |

analysis and only detects a depth of ∼5 nm while EDS is capable of measuring ∼1 μm depth, the difference means that chromium is more concentrated on the LSCF top surface (surface in contact with AISI 441), not through the bulk yet. This might also partly explain why no new phases can be detected at the AISI 441/LSCF interface.

Another observation from Table 2 is consistently higher Cr concentrations for the LSCF 95 and LSCF 105 samples. The A-site deficient electrode (LSCF 95) displays the smallest resistance to Cr diffusion while the stoichiometric LSCF contains the lowest Cr content. This phenomenon indicates that the distortion of the perovskite structure (non-stoichiometry) promotes Cr diffusion during the thermal treatment.

### 3.4. Interaction mechanisms between AISI 441 and LSCF cathodes

The cathode evolution and interaction mechanisms with the AISI 441 interconnect during the thermal treatment can be understood from the resistance change, the microstructural evolution, and the elemental re-distribution.

During the EIS test, the ohmic resistance of the cathode is governed by small polaron conduction (i.e. adiabatic-hopping of p-type polaron: $X^{4+}$) [18,34]; the low frequency arc in the impedance spectra is attributed to oxygen adsorption and dissociation as well as its surface diffusion [2]; and the high frequency arc corresponds to $O^{2-}$ incorporation into the electrode and its transport in the cathode [2]. Gas diffusion is negligible in this work as the porosities of the electrodes are sufficiently high (i.e. ∼40%).

Theoretically, the concentration of small polarons increases with $Sr^{2+}$ [18,34]. As this A-site species increases, some $X^{3+}$ ions should be oxidized to form $X^{4+}$ [18], which should improve the electrical conductivity of the electrode. However, at the very beginning, it seems that the $Sr^{2+}$ difference from the stoichiometry is small and become negligible when considering the microstructure difference. As shown in Fig. 1c, the connectivity of the porous LSCF networks decreases from LSCF 95 to LSCF 100 and to LSCF 105. This indicates loss of pathway for polarons with A-site excessive perovskite structure. As a result, the initial ohmic resistance increases from LSCF 95, to LSCF 100, and to LSCF 105.

The initial low frequency polarization resistance can also be understood based on the microstructure difference. The finer grains in the A-site deficient electrode (LSCF 95) provide a higher surface area and promote the oxygen adsorption/dissociation and the surface diffusion. Therefore, the initial $R_L$ continuously increases with A-site content increase.

The analysis on the initial high frequency polarization resistance, which is related to the number of oxygen vacancies and ultimately the corresponding diffusion rate, is more complicated. As mentioned above, $Sr^{2+}$ ions can introduce either $X^{4+}$ ions or oxygen vacancies to balance the perovskite structure. Although it is hard to estimate the exact number of oxygen vacancies generated by $Sr^{2+}$ ions, it can be certain that the amount decreases from A-site excessive electrode to A-site deficient electrode. On the other hand, the A-site deficiency itself (regardless of $Sr^{2+}$ presence on the A-site or not) would generate more oxygen vacancies than the stoichiometric electrodes. In addition, microstructure connectivity can also influence the oxygen diffusion. Since the porosity for each cathode is about the same, larger grains are beneficial for oxygen vacancy

diffusion (increasing oxygen vacancy diffusion rate from LSCF 95 to LSCF 100 and then to LSCF 105). However, fewer or shorter grain boundaries can compromise this trend. Because the stoichiometric difference among the studied electrodes involves these competing factors, it is difficult to estimate the exact oxygen vacancy diffusion trend in the three cathodes. Our conjecture is that, at the very beginning of the thermal treatment, LSCF 100 should have the highest oxygen vacancy diffusion rate because of its balanced properties: moderate A-site occupation, number of oxygen vacancies, and microstructure connectivity. The high frequency polarization resistance values listed in Table 1 confirm this assumption.

The electrochemical behaviors of the LSCF-based cathode during the thermal treatment are influenced by both the material diffusion through the tri-layer structure and the cathode microstructure changes. The evolution of different resistance values during the thermal treatment can be understood from these two aspects. The microstructural changes are clearly visible by comparing Figs. 1c and 4. The composition changes deserve more explanation. As discussed in section 3.3.2 (Figs. 5 and 6), the areas rich in Cr are also rich in Sr. This is consistent with prior studies that Cr deposition on LSCF electrode tends to form $SrCrO_4$ [3,35]. Although $SrCrO_4$ crystal phase was not detected by our XRD measurement, this EDS evidence supports the formation of $SrCrO_4$. In contrast, the locations rich in Fe are also rich in La (the Fe presence in LSCF itself leads us to believe that Fe diffusion from AISI 441 to LSCF is minimal and the Fe distribution locations in Figs. 5 and 6 support this). These phenomena indicate that Cr deposition tends to remove Sr from the perovskite crystal structure by the $SrCrO_4$ formation, and correspondingly Co also comes out of the crystal structure to balance the $ABO_{3-\delta}$ perovskite structure. The extraction of $Sr^{2+}$ from the perovskite structure leads to less increase in oxygen vacancies and $X^{4+}$ polarons. These factors jointly dictate resistance changes.

LSCF 95 cathode ohmic resistance decrease with thermal treatment time can be explained as follows. Comparing Figs. 5 and 6, it can be seen that Cr content is more dispersed in the A-site deficient electrode (LSCF 95) than in the A-site excessive electrode (LSCF 105). Cr distribution in LSCF 95 also has some overlapping regions with element La. Since La species always sits in A-site, this evidence suggests that Cr takes some A-sites in LSCF 95. It means that $Cr^{3+}$ participates in the LSCF perovskite structure instead of solely extracting $Sr^{2+}$ to form $SrCrO_4$, which is confirmed by the consistently high Cr concentration in Table 2. This general contribution of $Cr^{3+}$ to the perovskite structure implicates that there is less $Sr^{2+}$ being extracted from the A-site, which consequently suggests less decrease of oxygen vacancies and $B^{4+}$ polarons caused by Cr diffusion. Another look in elemental distribution is related to Co. In comparison, Co is much more widely distributed in LSCF 95 than in LSCF 100 and LSCF 105. Since less $Sr^{2+}$ is extracted from the perovskite crystal, less Co will come out of the crystal to balance the perovskite structure. All these point to the fact that the elemental diffusion exerts the smallest influence on LSCF 95 electrical conductivity. From a different perspective, among all three electrodes, LSCF 95 experiences the most dramatic microstructure evolution (throughout the cathode). Comparing Figs. 1c and 4, the connectivity of the porous network for LSCF 95 greatly improves after the thermal treatment, even though the grain sizes decrease. Therefore, the effect of the microstructure evolution counteracts the small elemental re-distribution effect on the electrical conductivity. Overall, this leads to a decrease in ohmic resistance with the thermal treatment time.

Since the diffusion of Cr in LSCF 95 leads to filling of the A-sites in the perovskite structure, it tends to bring the lattice back to regular perovskite crystal structure. This should facilitate the oxygen ion incorporation into the perovskite structure and

**Table 3**
Relationships between mechanisms of LSCF electrode evolution and resistance changes during the thermal treatment.

| | $R_\Omega$ | $R_H$ | $R_L$ |
|---|---|---|---|
| Governing mechanism | Small polaron hopping & Grain connectivity | $O^{2-}$ incorporation into electrode & diffusion | $O^2$ adsorption/dissociation & surface diffusion |
| LSCF 95 | $Cr^{3+}$ diffuses into A-site → less loss of $X^{4+}$ → charge carriers maintained; grain connectivity increase → $R_\Omega$ ↓ | $Cr^{3+}$ diffuses into A-site to maintain perovskite structure → improves oxygen incorporation and diffusion → $R_H$ ↓ | Grain boundary area increase → improvement of $O_2$ adsorption and diffusion → $R_L$ ↓ |
| LSCF 100 | $Sr^{2+}$ extracted by $Cr^{3+}$ → $X^{4+}$ decreases → $R_\Omega$ ↑; Grain connectivity increases → $R_\Omega$ ↓; $R_\Omega$ slightly decreases then stabilizes | $Sr^{2+}$ extracted by $Cr^{3+}$, $Co^{2+}$ displacement, and Cr deposition → compromises oxygen incorporation and diffusion → $R_H$ ↑ | Grain boundary area increase → improvement of $O_2$ adsorption and diffusion → $R_L$ ↓ |
| LSCF 105 | $Sr^{2+}$ extracted by $Cr^{3+}$ → $X^{4+}$ decreases → $R_\Omega$ ↑ (dominant); Grain connectivity increase → $R_\Omega$ ↓; $R_\Omega$ slowly increases | $Sr^{2+}$ extracted by $Cr^{3+}$, $Co^{2+}$ displacement, and Cr deposition → compromises oxygen incorporation and diffusion → $R_H$ ↑ | Grain boundary area increase → improvement of $O_2$ adsorption and diffusion → $R_L$ ↓ |

consequently the $O^{2-}$ diffusion through the electrode. As a result, the high frequency polarization resistance of LSCF 95 decreases with the thermal treatment.

The low frequency polarization resistance change for LSCF 95 should be understood by microstructure evolution as it is only related to oxygen adsorption/dissociation and surface diffusion. After the EIS test (Figs. 1c and 4a), the grain boundary area increases significantly as the grain size decreases. Therefore, the low frequency polarization resistance of LSCF 95 decreases during the thermal treatment.

LSCF 100 has an intermediate extent of microstructure evolution and elemental diffusion/re-distribution. Its stabilized ohmic resistance and slightly increased high frequency polarization resistance are the balancing results of these two phenomena. During the thermal treatment, diffusion of Cr causes loss of $Sr^{2+}$ and subsequently $X^{4+}$ ions, which tends to increase the ohmic resistance. However, the connectivity of the network is improved (even though the grain sizes of LSCF 100 are also reduced after the EIS test). Due to the competition of these different factors, the ohmic resistance only changes slightly. In addition, LSCF 100 is the most Cr-diffusion resistant composition among the three electrodes during the 100 h of thermal treatment (lowest Cr content shown in Table 2). This phenomenon may suggest that the diffusion of Cr slows down with time and could probably explain the stabilization of ohmic resistance. As to the high frequency polarization resistance, extraction of $Sr^{2+}$ by Cr and displacement of $Co^{2+}$ from the perovskite crystal structure adversely affect the oxygen incorporation into the cathode and the subsequent diffusion; the particle-like deposition of Cr on the cathode surface also likely blocks the available LSCF surface for $O^{2-}$ incorporation into LSCF 100 and transport after that. As a result, the high frequency polarization resistance increases for LSCF 100 with the thermal treatment. Similar to LSCF 95, the low frequency polarization resistance of LSCF 100 decreases with time, since the grain boundary area of the electrode increases after the EIS test and the oxygen adsorption/surface diffusion are correspondingly improved.

For LSCF 105, the changes of its ohmic resistance can be similarly explained by the above analysis. Specifically, with Sr content being extracted out from the perovskite structure, concentration of $Sr^{2+}$-induced $X^{4+}$ polarons continuously decreases. This loss of small polarons results in a decrease in the electrical conductivity and an increase in the ohmic resistance. Compared to LSCF 100, LSCF 105 has a higher Cr concentration, which indicates that more $Sr^{2+}$ is consumed by Cr and greater increase in ohmic resistance is expected. Therefore, the relatively small improvement in the microstructure connectivity of LSCF 105 is not able to counter this effect. For the increase in high frequency polarization resistance, the causes are similar as for LSCF 100. The leaching of $Sr^{2+}$ and $Co^{2+}$ from the perovskite crystal structure, which adversely affects the oxygen incorporation into the cathode and the subsequent

diffusion, and the particle-like deposition of Cr on the cathode surface, which likely blocks the available LSCF surface, contribute to the increase. The low frequency polarization resistance decrease for LSCF 105, again, is primarily related to microstructural changes. Although the microstructure evolution of this electrode is less significant compared to the other two LSCFs, the grain size decrease and grain boundary area increase still lead to enhanced oxygen adsorption/dissociation and surface diffusion and thus low frequency polarization resistance decrease.

The mechanisms of the LSCF evolution and contribution to the electrochemical behaviors during the thermal treatment are summarized in Table 3. It should be mentioned that the Pt wire and Pd paste used in this study might form intermetallics in the studying condition. The corresponding influence on the EIS spectra is not yet confirmed.

## 4. Conclusions

LSCF powders with different stoichiometries are used to create AISI 441/LSCF/YSZ tri-layer half-cells in order to study the material degradation issues during solid oxide fuel cell use at 800 °C under current load. LSCF microstructure evolution, AISI 441/LSCF interfacial elemental diffusion and re-distribution along with their relations to the LSCF stoichiometry, and the correspondingly half-cell electrochemical behaviors are discussed. The thermal treatment results in dramatic microstructure evolution and influences the electrochemical behaviors of the cathodes. Chromium diffusion into the LSCF electrodes is mostly concentrated at the AISI 441/LSCF interface. The ohmic resistance, high frequency polarization resistance, and low frequency polarization resistance are analyzed by fitting the impedance spectra. The electrochemical performance of the cathodes is a combined result of microstructure evolution and elemental diffusion. The mechanisms for the above processes are proposed. Overall, the A-site deficient stoichiometry (LSCF 95) is preferred as it shows the smallest overall resistance for a long period when used as a cathode.

## Appendix A. Supplementary data

Supplementary data related to this article can be found at http://dx.doi.org/10.1016/j.jpowsour.2013.03.012.

# References

[1] W.Z. Zhu, S.C. Deevi, Mater. Sci. Eng. A. 348 (2003) 227—243.
[2] Z.Y. Jiang, L. Zhang, K. Feng, C.R. Xia, J. Power Sources 185 (2008) 40—48.
[3] S.P. Jiang, Y.D. Zhen, Solid State Ionics 179 (2008) 1459—1464.
[4] S.J. Skinner, J.A. Kilner, Solid State Ionics 135 (2000) 709—712.
[5] S.B. Adler, Chem. Rev. 104 (2004) 4791—4843.
[6] J.M. Vohs, R.J. Gorte, Adv. Mater. 21 (2009) 943—956.
[7] W.G. Wang, M. Mogensen, Solid State Ionics 176 (2005) 457—462.
[8] F.S. Baumann, J. Fleig, H.U. Habermeier, J. Maier, Solid State Ionics 177 (2006) 1071—1081.
[9] J. Mizusaki, J. Tabuchi, T. Matsuura, S. Yamauchi, K. Fueki, J. Electrochem. Soc. 136 (1989) 2082—2088.
[10] Z.G. Lu, J. Hardy, J. Templeton, J. Stevenson, J. Power Sources 198 (2012) 90—94.
[11] Y. Takeda, R. Kanno, M. Noda, Y. Tomida, O. Yamamoto, J. Electrochem. Soc. 134 (1987) 2656—2661.
[12] E.Q. Zhao, Z. Jia, L. Zhao, Y.P. Xiong, C.W. Sun, M.E. Brito, J. Power Sources 219 (2012) 133—139.
[13] Y. Zeng, Y.S. Lin, S.L. Swartz, J. Membr. Sci. 150 (1998) 87—98.
[14] S. Hashimoto, Y. Fukuda, M. Kuhn, K. Sato, K. Yashiro, J. Mizusaki, Solid State Ionics 186 (2011) 37—43.
[15] E. Konysheva, H. Penkalla, E. Wessel, J. Mertens, U. Seeling, L. Singheiser, K. Hilpert, J. Electrochem. Soc. 153 (2006) A765—A773.
[16] Y. Matsuzaki, I. Yasuda, J. Electrochem. Soc. 148 (2001) A126—A131.
[17] H. Hwang, G.M. Choi, J. Electroceram. 22 (2009) 67—72.
[18] L.W. Tai, M.M. Nasrallah, H.U. Anderson, D.M. Sparlin, S.R. Sehlin, Solid State Ionics 76 (1995) 273—283.
[19] E.P. Murray, M.J. Sever, S.A. Barnett, Solid State Ionics 148 (2002) 27—34.
[20] H. Ullmann, N. Trofimenko, F. Tietz, D. Stover, A. Ahmad-Khanlou, Solid State Ionics 138 (2000) 79—90.
[21] A. Mai, V.A.C. Haanappel, S. Uhlenbruck, F. Tietz, D. Stover, Solid State Ionics 176 (2005) 1341—1350.
[22] A. Mineshige, J. Izutsu, M. Nakamura, K. Nigaki, J. Abe, M. Kobune, S. Fujii, T. Yazawa, Solid State Ionics 176 (2005) 1145—1149.
[23] R. Doshi, V.L. Richards, J.D. Carter, X.P. Wang, M. Krumpelt, J. Electrochem. Soc. 146 (1999) 1273—1278.
[24] D. Waller, J.A. Lane, J.A. Kilner, B.C.H. Steele, Solid State Ionics 86 (1996) 767—772.
[25] H.Y. Tu, U. Stimming, J. Power Sources 127 (2004) 284—293.
[26] D. Oh, D. Gostovic, E.D. Wachsman, J. Mater. Res. 27 (2012) 1992—1999.
[27] J.A. Schuler, Z. Wuillemin, A. Hessler-Wyser, C. Comminges, N.Y. Steiner, J. Van Herle, J. Power Sources 211 (2012) 177—183.
[28] S. Taniguchi, M. Kadowaki, H. Kawamura, T. Yasuo, Y. Akiyama, Y. Miyake, T. Saitoh, J. Power Sources 55 (1995) 73—79.
[29] S.P.S. Badwal, R. Deller, K. Foger, Y. Ramprakash, J.P. Zhang, Solid State Ionics 99 (1997) 297—310.
[30] S.P. Jiang, Solid State Ionics 146 (2002) 1—22.
[31] S.G. Li, W.Q. Jin, N.P. Xu, J. Shi, Solid State Ionics 124 (1999) 161—170.
[32] T.G. Jin, K. Lu, Int. J. Hydrogen Energy 36 (2011) 4440—4448.
[33] Y.J. Leng, S.H. Chan, S.P. Jiang, K.A. Khor, Solid State Ionics 170 (2004) 9—15.
[34] L.W. Tai, M.M. Nasrallah, H.U. Anderson, D.M. Sparlin, S.R. Sehlin, Solid State Ionics 76 (1995) 259—271.
[35] S.P. Jiang, S. Zhang, Y.D. Zhen, J. Electrochem. Soc. 153 (2006) A127—A134.